Three-dimensional effects in low Reynolds number flow around confined cylinders

Vera M. Ribeiro[1], Hugo E. Ferreira[2,3], Patrícia C. Sousa[1], Paulo M. Coelho[3], Fernando T. Pinho[4,5], Manuel A. Alves[1]

1: CEFT, Departamento de Engenharia Química, Faculdade de Engenharia da Universiade do Porto, Porto, Portugal, vera@fe.up.pt, psousa@fe.up.pt, mmalves@fe.up.pt
2: DEMGI, Escola Superior de Tecnologia, Instituto Politécnico de Viseu, Viseu, Portugal, hugomoreira@estv.ipv.pt
3: CEFT, Departamento de Engenharia Mecânica, Faculdade de Engenharia da Universidade do Porto, Porto, Portugal, pmc@fe.up.pt
4: Centro de Estudos de Fenómenos de Transporte (CEFT), Faculdade de Engenharia da Universidade do Porto, Porto, Portugal, fpinho@fe.up.pt
5: Universidade do Minho, Largo do Paço, Braga, Portugal

Abstract An experimental and numerical study is carried out to investigate three-dimensional effects in the flow of Newtonian fluids around confined cylinders, for Reynolds numbers below 40 and aspect ratios between 1 and 16. Experiments rely on flow visualizations and detailed velocity measurements by PIV, while predictions were carried out using a finite volume method. Velocity peaks near the side walls were found to occur at all Reynolds numbers and for $AR > 3$. At low Reynolds numbers these velocity peaks are due to the excessive braking role of the side wall, which forces a local fluid acceleration for mass conservation that the very small diffusive spanwise-streamwise momentum flux (τ_{xz}) is unable to smooth out. This disappears when the aspect ratio is reduced and by implication the τ_{xz} stress increases strongly. Inertia counteracts the role of this diffusive momentum flux so much that at $AR = 1$ there are still velocity peaks when $Re = 40$. When inertia is strong there is flow separation in the wake of the cylinder, but this separated flow region is open. The fluid particles near the side wall, but not too near, are better able to sustain the adverse streamwise pressure gradient and recover better the pressure as they flow across the cylinder. Consequently, the separated flow region is shorter and the pressure is higher in that region leading to a secondary spiraling spanwise flow from the side wall to the centre plane. The fluid exits the recirculation region at the centre plane and enters it at the velocity peak region near the wall, which is being fed by fluid coming from the neighbour region located to the inner side of the duct. This has a positive feedback enhancing the velocity peaks. At the wall itself friction extracts so much energy from the fluid particles that these are less able to sustain the adverse streamwise pressure gradient and the separated flow length increases significantly.

1. Introduction

The two-dimensional sub-critical steady laminar flow around a confined cylinder with a blockage ratio of 50% is an established benchmark in the development of numerical methods for non-Newtonian fluids, especially those exhibiting viscoelasticity (Brown and McKinley, 1994). However, the practical implementation of such a flow is indeed three-dimensional (Verhelst and Niewstadt, 2004) and the combination of flow inertia, viscoelasticity and three-dimensionality often leads to surprising results, such as the appearance of unexpected velocity peaks near the side walls in profiles taken along the *neutral direction* of the flow, as was recently discovered in the context of another flow having some common characteristics with the confined cylinder in a rectangular channel (e.g. Poole et al, 2007). This and the resurgence of laminar flows in 3D geometries of low aspect ratios, so typical of microfluidics, motivated a research program onto low Reynolds number laminar flows around cylinders confined in rectangular ducts in order to investigate the magnitude of three-dimensional effects.
Research on 3D effects in confined steady cylinder flows is relatively recent and partially stems

from their use as benchmark flows for viscoelastic fluids without geometric singularities. Not surprisingly, most investigations are numerical such as by Carew and Townsend (1991), Anagnostopoulos et al (1996) or Alves et al (2001). Another motivation is the existence of such confinements and obstacles in flows of relevance to polymer extrusion and injection molding, where the Reynolds numbers are quite low by virtue of the high fluid viscosity.
Three-dimensional effects in cylinder Newtonian flows have been extensively studied in the turbulent regime, as in Gerich and Eckelman (1982) and Norberg (1994). Also, under laminar flow conditions vortex shedding starts at Reynolds numbers of around 47 and here 3D effects are crucial to the onset of a second bifurcation at $Re \sim 200$ (Williamson, 1996). These are still a hot research topic using modern numerical techniques (for instance, lattice Boltzmann as in Liu, 2008). These investigations on the bifurcations from steady to periodic to unsteady flow essentially concentrate on the effect of aspect ratio at low blockage ratios.
In this work an experimental and numerical investigation is conducted on the Newtonian flow around a confined cylinder in a rectangular duct at a high blockage ratio of 50% and at Reynolds numbers below the critical value for the onset of vortex shedding aimed at investigating three-dimensional effects.
The test rig and instrumentation are described in Section 2, which ends with a brief explanation of the numerical method. Comparisons between experiments and computations are shown first in Section 3, where a discussion of these sets of results is also made. Subsequent results of the 3D effects from detailed extensive numerical calculations are presented afterwards and prior to closure.

2. Test rig, instrumentation and numerical method

The test rig is a closed system schematically represented in Figure 1, which was put inside a dark room for the flow visualizations. The 10 mm diameter (D) cylinder is inside a 1.7 m long duct with a rectangular cross-section having a depth (H) of 20 mm and a variable width (L). The cylinder is located 0.63 m downstream of the distributor located at the rectangular duct inlet, and is positioned at the mid plane to define a symmetric geometry with a 50% area blockage (D/H). The width of the rectangular duct and cylinder can be varied to assess the effect of the aspect ratio ($AR = L/H$) between 1 and 8, but experimental results are here presented only for $AR = 8$. Throughout the paper the duct aspect ratio is used; the cylinder aspect ratio is twice the duct aspect ratio. The feeding distributor has six large diameter injectors to ensure as much as possible a uniform velocity profile at the inlet. The flow rate is set by gravity between the two free surfaces of the inlet R1 reservoir and the discharge tank R2, which is standing on a balance. The two reservoirs are pressurized to reduce the chances of air entrainment into the rig and to avoid the formation of small bubbles in regions of low pressure. A centrifugal pump Cp in the return line closes the circuit with a one-way valve. This pump is switched off for a few seconds when the main flow rate is measured at the balance (maximum bulk velocities in the channel never exceeded 0.01 m/s).
The Reynolds number based on the duct bulk velocity and cylinder radius (R) was varied up to 40 in order to maintain steady flow. The range of Reynolds numbers investigated is such that the flow becomes fully-developed well before the cylinder and the exit is sufficiently far form the cylinder not to affect the flow dynamics in the vicinity of the cylinder. All flows were steady and symmetric as will be confirmed by the experimental and numerical results. All experiments were carried out with water.
Experiments relied on flow visualization and particle image velocimetry (PIV). The flow visualizations used laser illumination from two co-planar 635 nm 5 mW laser diodes (L1 and L2) to eliminate shadows. The laser diodes were fitted with cylindrical lens to create a light sheet and a digital camera (CANON EOS 30D with a macro EF100mm f/2.8 lens) took the pictures. The suspended PVC particles that provided the stream traces had a diameter of 10 μm and exposure

times varied from 1 to 30s, depending on flow velocity.
Detailed velocity measurements were carried out using a PIV system. The flow plane under investigation was illuminated by a double pulsed Nd:YAG laser with a maximum energy of 50 mJ per pulse (Solo PIV III, New Wave Research) and the images were acquired through a digital CCD camera having a resolution of 1600 by 1186 pixels (Flow Sense 2M, Dantec Dynamics) coupled with a 60 mm lens (Nikon AF Micro). These and the location of the camera defined a scale factor, which varied between 5.888 and 15.015.

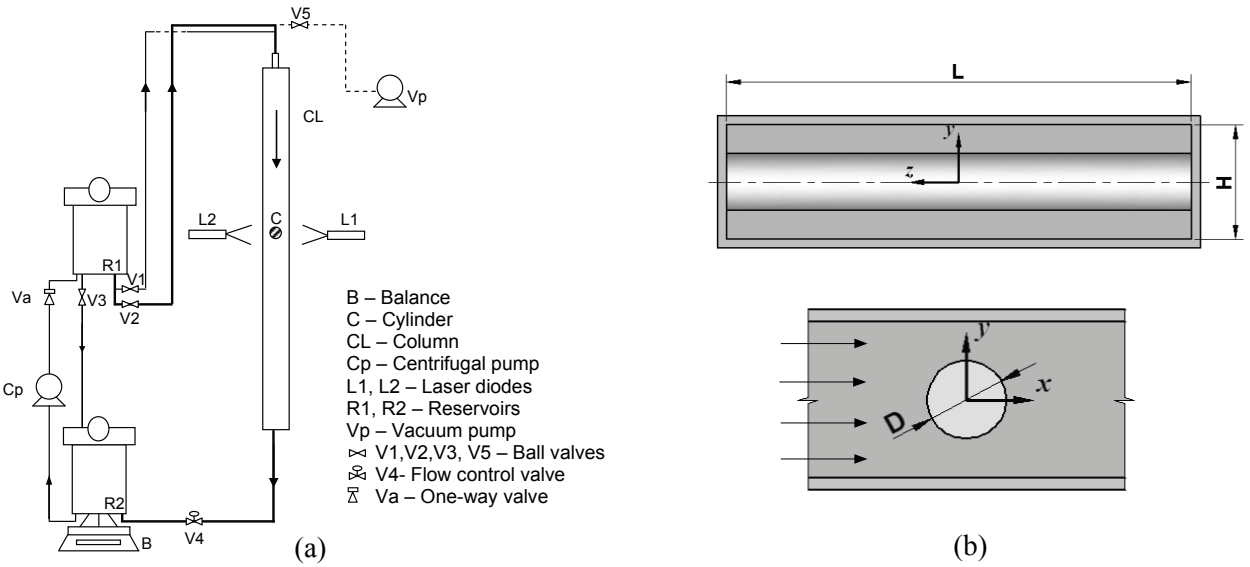

Figure 1 - Schematic representation of the experimental set-up: (a) the rig; (b) test section cross-section and coordinate system (main flow is along *x*-direction).

The mean velocity profiles from PIV were obtained with data averaging from 50 image pairs. Time between pulses was varied between 14 ms and 2.3 s depending on the flow conditions and the scaling factor. The images were acquired and post-processed by FlowManager v4.60 software from Dantec Dynamics using adaptive correlation on interrogation windows ranging between 64 by 64 pixels to 16 by 16 pixels, depending on the plane of measurement, with 50% overlap. For the uncertainty analysis the sub-pixel interpolation had random and systematic uncertainties of ± 0.74 μm (± 10%) and ± 0.21 μm, respectively leading to ± 0.77 μm total uncertainty for the particle motion. This resulted in absolute uncertainties of ± 0.33 mm/s for the larger velocities and of ± 26 μm/s for the lower velocities. The maximum relative uncertainty was of the order of ± 5% of the local velocities.
The numerical calculations of the 3D laminar flow were carried out using a finite-volume code, which has been extensively used and validated (Oliveira et al 1998, Alves et al 2001). These references explain the numerical method in detail, hence here only a brief description is presented. The numerical method is based on the time-marching version of the SIMPLEC pressure correction algorithm formulated for collocated variables by Issa and Oliveira (1994). The continuity and Navier-Stokes equations for the Cartesian velocity vector written in non-orthogonal coordinates are integrated in space over each of the computational cells of volume V_P of the mesh, and in time over a time step (Δt), to form sets of linearized algebraic equations. The discretization of the governing equations is based on central differences for diffusion terms and for the convective terms the interpolating scheme employed is the CUBISTA high resolution scheme (Alves et al, 2003), formally of third order accuracy in uniform meshes.
The full domain was mapped by block-structured meshes. The inlet and outlet were located 200 and 140 cylinder radii upstream and downstream of the origin of the coordinate system, respectively, to allow complete flow development well before the effect of the cylinder is felt and to eliminate

outlet boundary condition effects in the region of interest. To generate the mesh the flow domain was divided into 24 blocks and within each block the cells were concentrated near the cylinder region, as represented in Figure 2. Extensive sets of calculations were carried out by Ferreira (2006) to estimate the numerical uncertainty and select an adequate mesh to provide mesh independent results. The results presented in this work are characterized by $(\Delta l/R)_{min} = 0.034$, $(\Delta r/R)_{min} = 0.033$ and $(\Delta r/R)_{min} = 0.050$, where l is the arc around the cylinder surface and is equal to x elesewhere.

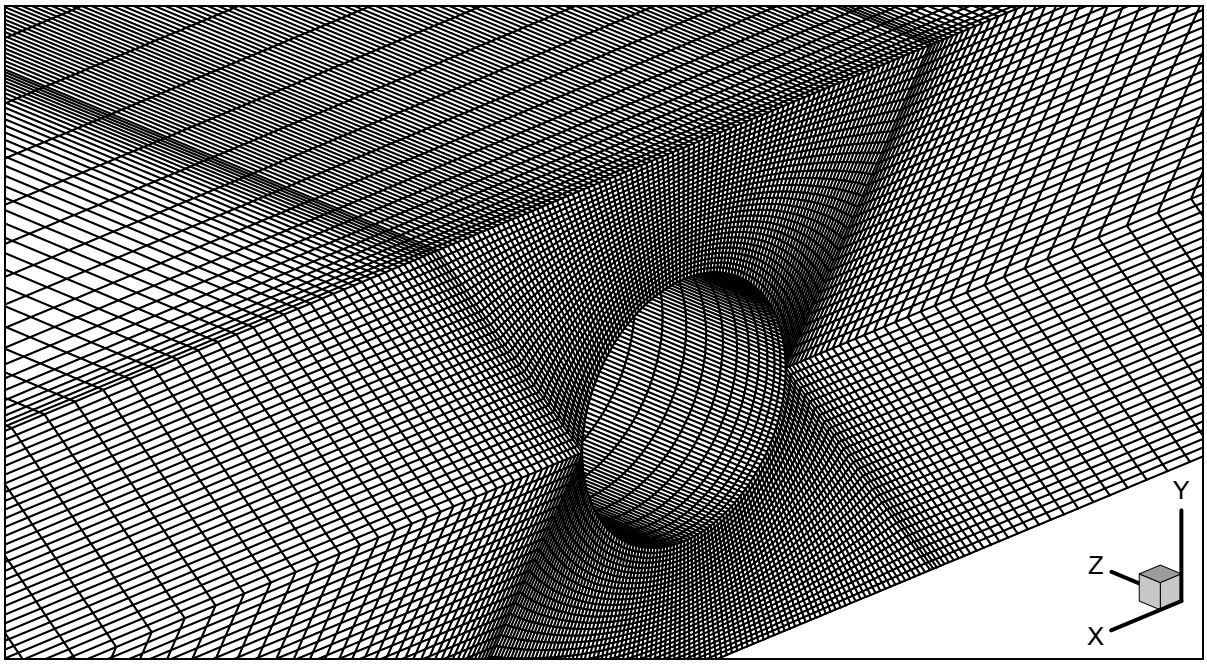

Figure 2 - Zoomed view of the mesh used in the vicinity of the cylinder.

3. Results and discussion

3.1 Main flow characteristics and validation

Figure 3-a) shows a streak line photo obtained during the flow visualization at $Re = 23.6$ to illustrate the quality of this set of measurements by flow visualization. Figure 3-b) compares the calculated and measured variation with Reynolds number of the dimensionless length of the cylinder vortex, at the $z/R = 0$ symmetry plane of the cylinder, for an aspect ratio of 8. The comparison between numerical results and streak line photography visualizations is good and shows the recirculation region appearing at Reynolds numbers above 6. This is an open recirculation and fluid particles move along the span wise direction in spiraling motion from the side walls towards the centre plane, as recently demonstrated in the numerical study of Ferreira (2006).

Figure 4 shows measured profiles of the normalized streamwise velocity along the centerline of the test section (coordinates $(x, 0, 0)$) at Reynolds numbers of 15.2 and 27.5. Upstream of the cylinder the two profiles coincide and show that in the core of the duct the approach flow is only affected by the presence of the cylinder within -4 cylinder radii. Downstream the cylinder the recirculation is well captured and the length of the recirculations, L_v, that are obtained from these experimental profiles match well the data from the flow visualization experiments. The lines in the figure represent the corresponding predicted profiles and it is clear that there is good agreement between experiments and numerical calculations.

Velocity profiles measured by PIV at $y/R = 0$ and $s/R = 2, 4, 6$ and 12 for $Re = 15.2$ and $AR = 8$ are

shown on the left-hand-side of Figure 5 and compare very well with the corresponding calculated profiles (s represents the distance to the rear stagnation point, $s/R = x/R - 1$). The plot on the right-hand-side of Figure 5 shows the same comparison at a higher Reynolds number, $Re = 27.5$. At low Reynolds numbers a small overshoot of axial velocity is already visible near the *neutral direction* wall ($|z/R| \rightarrow 16$), and the comparison between the two parts of Figure 5 indicates that the velocity overshoot is strongly enhanced with increasing flow inertia. The appearance of strong velocity overshoots downstream of the cylinder and near the side walls, in the mid plane, is a remarkable result. As shown on the right-hand-side of Figure 5, this overshoot propagates and is intensified in the near wake of the cylinder (they are stronger at $s/R = 4$ than at $s/R = 2$), before being dampened by diffusion. Still, for $Re = 27.5$ they are still visible at $s/R = 12$. The magnitude of these overshoots depend strongly on inertia, but they are also present at inertialess flow ($Re = 0$), although not so intense as will be seen. The variation of the recirculation region length with Reynolds number is also apparent in the comparison: at $s/R = 2$ the velocities are already positive for $Re = 15.2$ (smaller L_v), but are negative for $Re = 27.5$ (larger L_v).

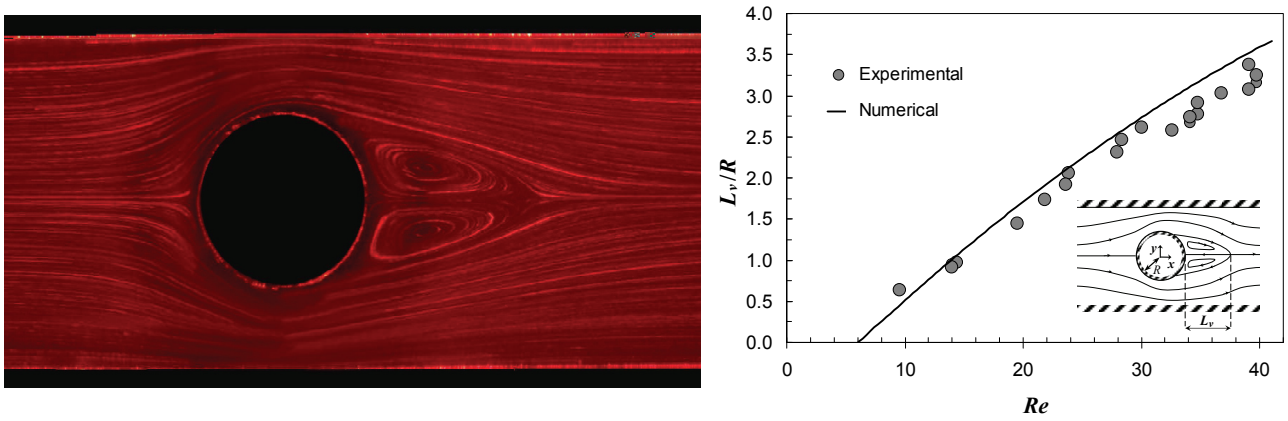

(a) (b)

Figure 3 - Results from visualizations at the z/R =0 mid plane: (a) Streakline photography at $Re = 23.6$; (b) Comparison between the measured and calculated cylinder vortex length.

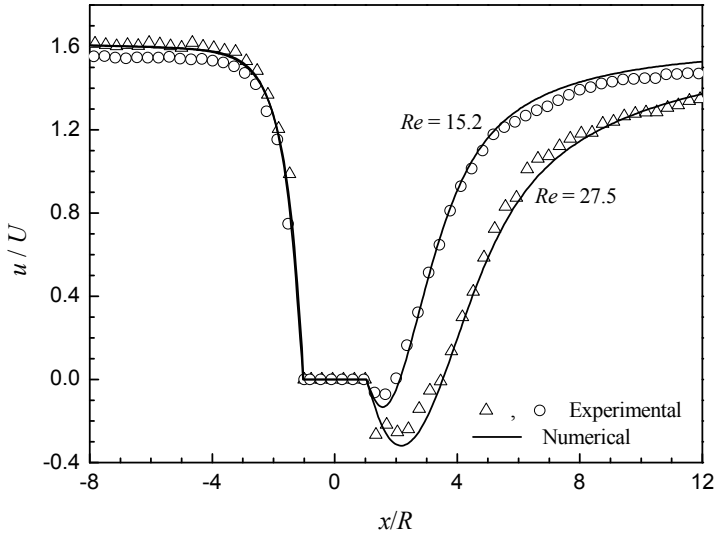

Figure 4 - Normalised axial velocity profiles along the centerline ($y/R = 0$, $z/R = 0$) for $Re = 15.2$ and 27.5.

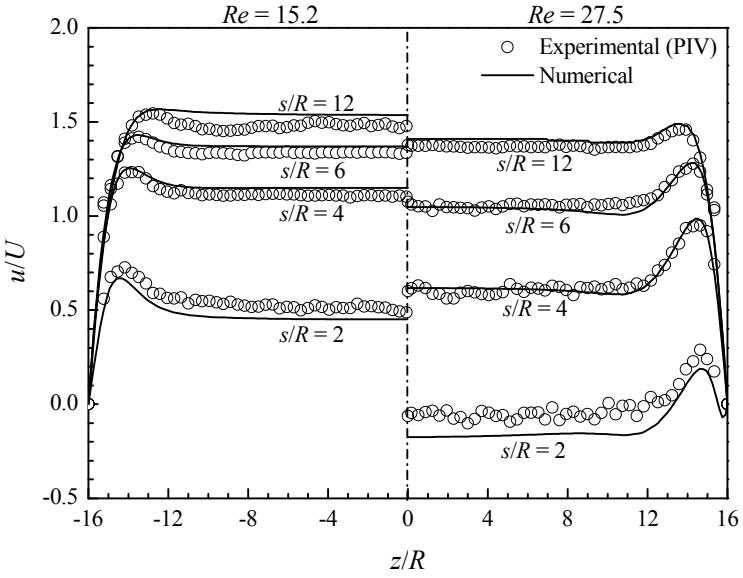

Figure 5 - Axial velocity along the *neutral* direction for a number of axial positions at $y/R = 0$ (s represents the distance to the rear stagnation point, $s/R = x/R - 1$).

Figures 6-a) and 6-b) show transverse profiles of the axial velocity upstream of the cylinder for $Re = 19.8$ at the centre plane ($z/R = 0$) and in the region of peak velocity ($z/R \cong 14$). The comparison with the corresponding predictions is fair with differences within experimental uncertainty. Since all profiles were symmetric only half-profiles are shown. Figure 6-a) includes the fully-developed profile predictions at $s/R = -10$ to help confirm that the presence of the cylinder has a small effect upstream of $x/R < -3$ all across the width and especially in the core as suggested by Figure 4. The finite span of the duct is felt in the normalised centerline velocity, which is equal to 1.629 in contrast to 1.5 for a 2D channel flow. The profiles of Figure 6-b) are closer to the cylinder, at $s/R = -2$, where its presence starts to be felt as a flow deceleration everywhere. Here, as at $s/R = -4$ the velocities are higher on the centre plane than near the side walls. The corresponding profiles downstream of the cylinder are shown in Figures 6-c) and 6-d) for $s/R = +2$ and $+4$, respectively. The presence of the cylinder is apparent in the wake and in the ensuing flow acceleration of the jet formed between the cylinder and the transverse wall. In contrast to the upstream profiles of Figures 6-a) and 6-b) now the profiles at $z/R = 14$ have higher velocities in the near wake than those at the $z/R = 0$ centre plane for $y/R < 0.8$. The higher wake velocities at $z/R = 14$ correspond to the streamwise velocity peaks reported in Figure 5. Therefore, this side wall jet is not only observed at $y/R = 0$, but is felt over nearly half the width of the channel. The predictions capture these effects nicely and actually compare better with experiments downstream of the cylinder than in the upstream profiles.

The comparison between experimental and numerical data of Figures 3 to 6 extensively validated the numerical calculations. Therefore, in what follows only numerical data are used to explore the dynamics of the flow and help interpret the causes for the velocity peaks. Figure 5 already showed that the velocity peaks near the side walls are a 3D effect that is significantly enhanced by flow inertia, but one peculiar characteristic at *high* Reynolds number flows so far unreported is shown in Figure 7-a). This figure shows calculated spanwise profiles of streamwise velocity downstream of the cylinder at various Reynolds numbers for $AR = 8$ using a fine mesh. The plots for $Re = 20$ and 40, corresponding to cases with a large separated flow region, show that next to the strong positive velocity peak there is a region of minimum velocity. This local velocity deficit is possibly due to fluid that feeds into the nearby jet.

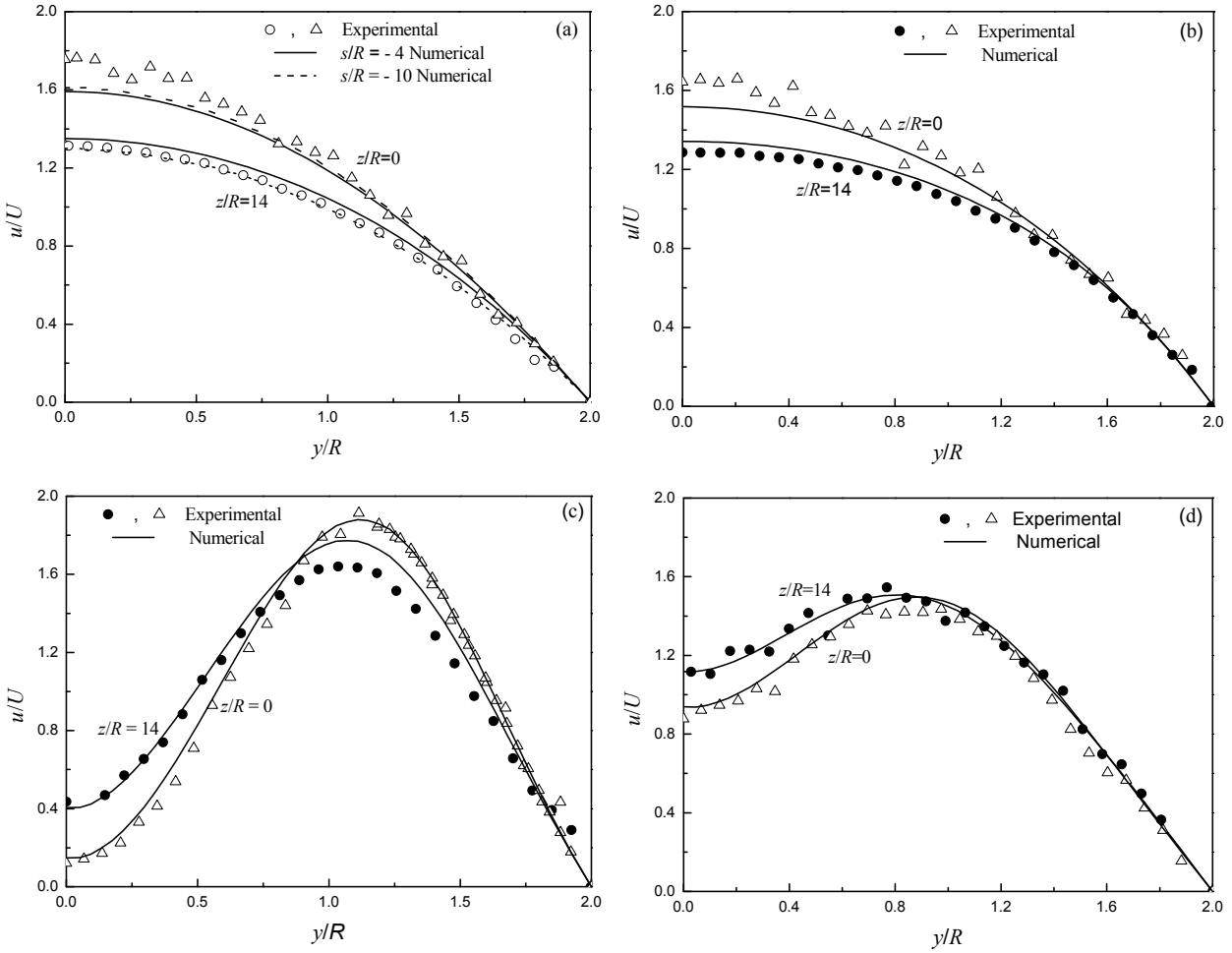

Figure 6 - Effect of spanwise coordinate on transverse profiles of axial velocity for $Re = 19.8$ at: (a) $s/R = -4$; (b) $s/R = -2$; (c) $s/R = +2$; (d) $s/R = +4$.

Velocity peaks are not exclusive of *high* Reynolds number flows and have been reported at $Re = 0.23$ by Verhelst and Niewstadt (2004). This is confirmed here in the numerically predicted spanwise profiles of streamwise velocity at $y/R = 0$ of Figure 7-b) for $Re = 0$. These profiles pertain to aspect ratios of 1, 4, 8 and 16 and show that at $Re = 0$ the effect is stronger for large values of AR. The velocity peaks tend to disappear for $AR < 3$, as the flow tends to Hele-Shaw ($AR \to 0$). Obviously, for $AR \to \infty$ the flow becomes two-dimensional with no velocity peaks. The shapes of the velocity profiles and of the velocity peaks at $Re = 0$ are different from those at *large* Reynolds number flows with separation in Figure 7-a), but not too different from the shape of the profile at $Re = 10$ in Figure 7-a).

Figures 8-a) and 8-b) show the calculated spanwise profiles of the length of the separated flow region corresponding to the flows of Figures 7-a) and 7-c). An increase in Reynolds number is characterized by an increase in L_v, as in Figure 3. Regarding the variation of L_v with z/R there is an inverse correspondence with the profiles of streamwise velocity with velocity jets corresponding to regions of low L_v and the region of small velocity deficit for the $AR = 8$ profiles showing a slightly longer L_v.

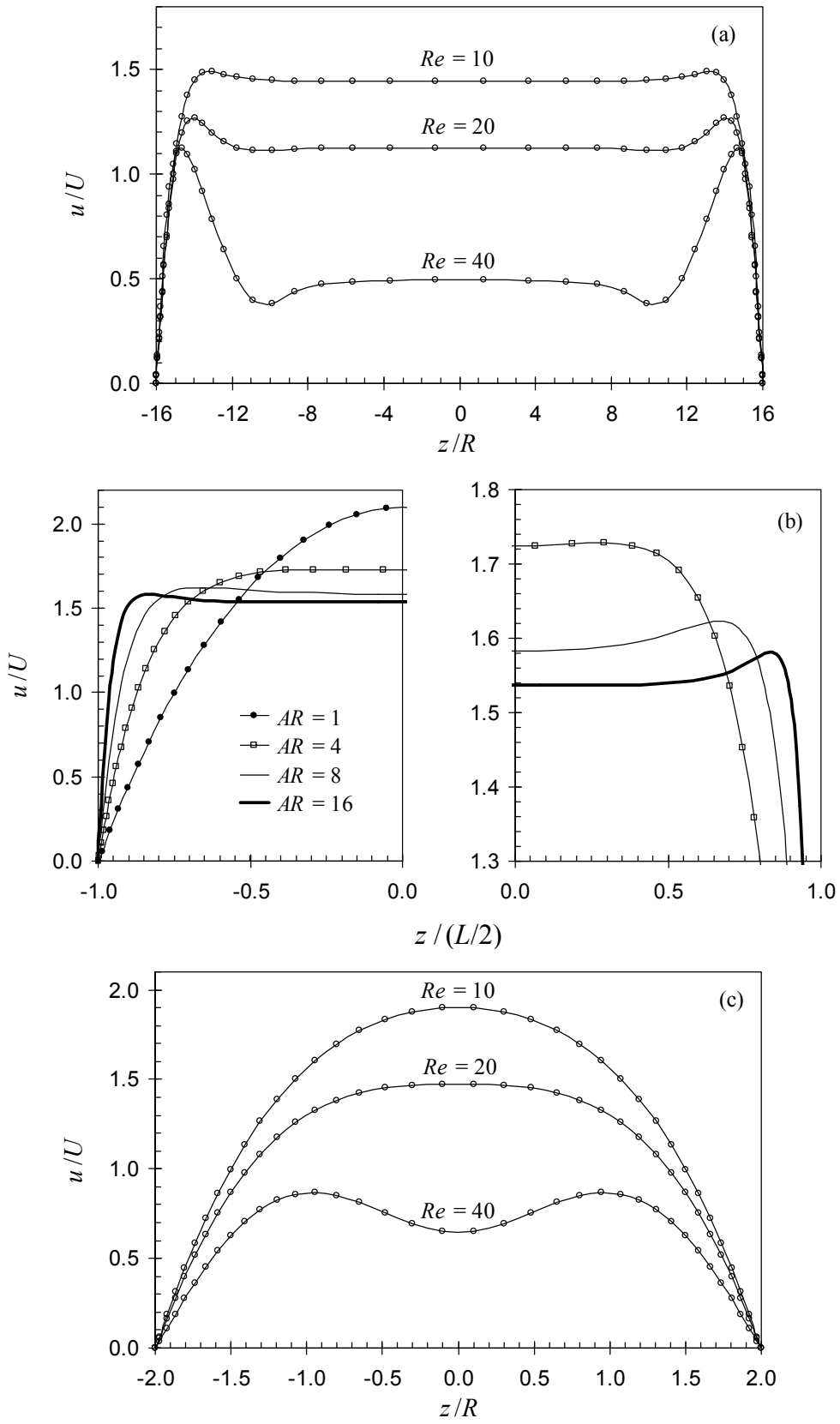

Figure 7 - Profiles of axial velocity at $y/R = 0$ and $s/R = 5$ as a function of spanwise coordinate for various aspect ratios and Reynolds numbers: (a) $10 \leq Re \leq 40$ and $AR = 8$ at $s/R = 6$; (b) $Re = 0$ and $AR = 8$; (c) $10 \leq Re \leq 40$ with $AR = 1$. In (b) a smaller range of u/U is also displayed in order to better illustrate the existence of small velocity overshoots under creeping flow conditions for large AR.

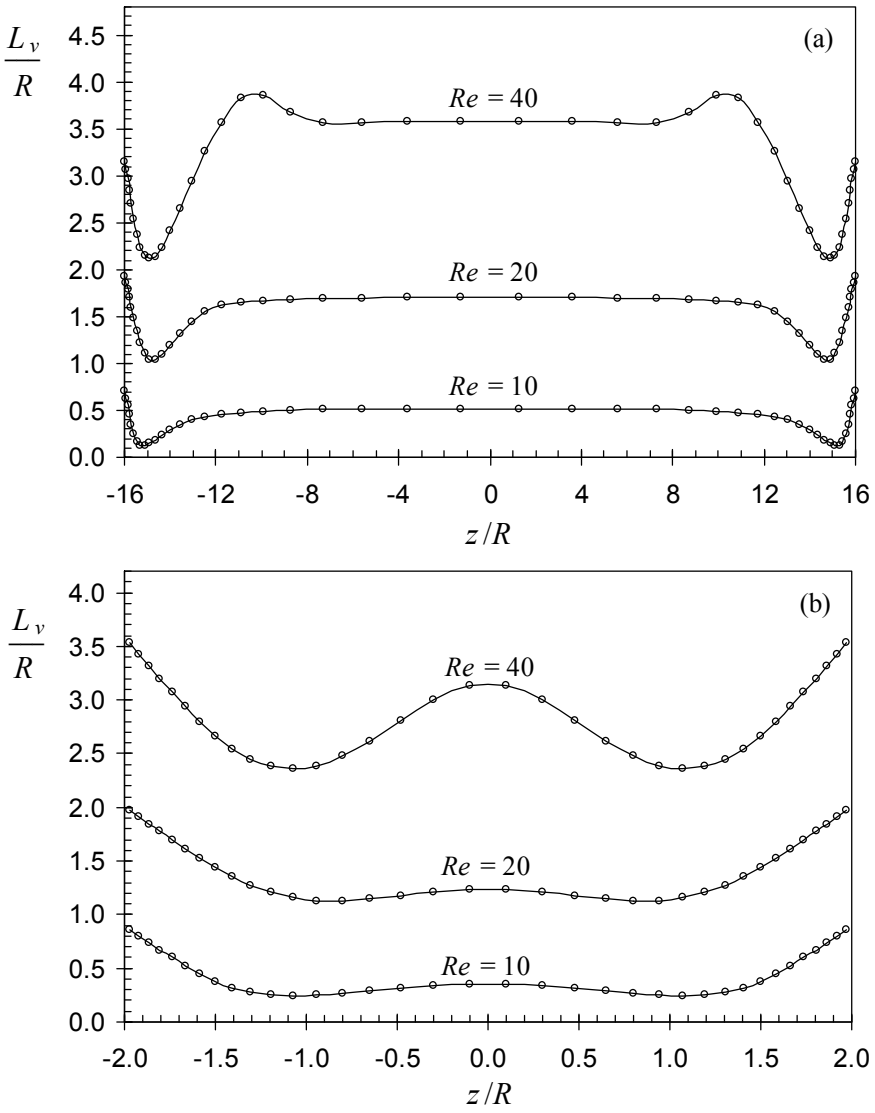

Figure 8 - Spanwise variation of recirculation length as a function of Reynolds number at $y/R = 0$: (a) $AR = 8$; (b) $AR = 1$.

3.2. A tentative mechanism for the velocity peaks

What are the causes for these velocity peaks in its various forms is discussed next. It is appropriate here to start with the creeping flow case at large aspect ratios. Fluid particles approaching the cylinder must accelerate to negotiate the obstacle, but the particles close to the side walls are slowed down by the presence of the walls and are less able to accelerate. Therefore, there is a corresponding localized acceleration at some distance from the wall to compensate for the flow slow down, which diffusion cannot smooth in the spanwise direction because the responsible momentum flux (τ_{xz}) is small (the wall is continuously slowing down fluid as particles move downstream). Consequently a velocity peak is formed. This is consistent with the location of the velocity peaks in Figure 7-b): in terms of $\Delta z/L$ the distance of the peaks to the side wall increase in inverse proportion to AR, but this corresponds to the same diffusion distance Δz. This picture is only changed by inertia which reduces the time available for τ_{xz} to act and for this reason the peak velocity at $Re = 10$ in Figure 7-a) is closer to the side wall than the peak at $Re = 0$, for the same value of AR.

As AR decreases the τ_{xz} stresses increase and this smoothes the peaks. For that reason in Figure 7-b) the velocity peaks not only move away from the side wall, as explained above, but the peaks also become less and less pronounced. Note that as $AR \to 0$ a Hele-Shaw flow is approached, and it becomes dominated by the large τ_{xz} stresses and the velocity variations across the spanwise direction will become parabolic, eliminating all localized velocity peaks. Inertia can counteract this effect and this is seen in Figure 7-c), in particular for $Re = 40$ where velocity peaks are seen. Figure 8-b) also confirms the role of inertia in counteracting the smoothing effect of the large τ_{xz} stresses.
As the Reynolds number increases this picture is perturbed by inertial effects, which become superimposed on the above mechanism. The following explanation is for large aspect ratios, such as $AR = 8$. A region of minimum recirculation length is observed to exist at the same location of the velocity peaks and this is especially obvious for flows with strong separation (cf. Figure 8-a)). At large Reynolds numbers the flow in the region of small L_v is able to negotiate the cylinder with minimum pressure loss, i.e., it is able to recover pressure more efficiently than fluid farther from the wall, and there are two causes for this. Its slowdown by the wall as it approaches the cylinder is not very strong, but it is sufficient to reduce locally the Reynolds number and this leads to a smaller recirculation length very much as the effect of Reynolds number depicted in Figure 3. Then, because it is acquiring fluid from the neighbor region of velocity deficit it gets extra energy to help sustain the adverse pressure gradient. Note that this fluid comes from upstream.
The better pressure recovery in the region of minimum L_v creates a spanwise pressure gradient leading to a spiraling secondary flow inside the open separated flow region from the side walls to the centre plane, a mechanism enhanced by flow inertia and illustrated in Figure 9. This secondary flow takes fluid out of the near side wall region and into the centreplane. Simultaneously fluid must enter this recirculation. The smaller recirculation constitutes a lesser obstruction to the flow, so that neighbor fluid on the inner side moves outwards to the small L_v region to feed this region and the open recirculation, creating at the same time a strong jet locally and depleting the neighbor region of fluid, which corresponds to the minimum in the spanwise velocity profiles of Figure 7-a) (velocity deficit) and correspondingly reduces its capability to sustain the streamwise adverse pressure gradient as it flows across the cylinder, hence the corresponding larger L_v in Figure 8-a). At large Reynolds numbers these inertial/ boundary layer mechanisms far outweigh the acceleration mechanism described earlier and the velocity peaks acquire their special sharp forms. Reducing aspect ratio brings into action the discussed smoothing effect of τ_{xz}.

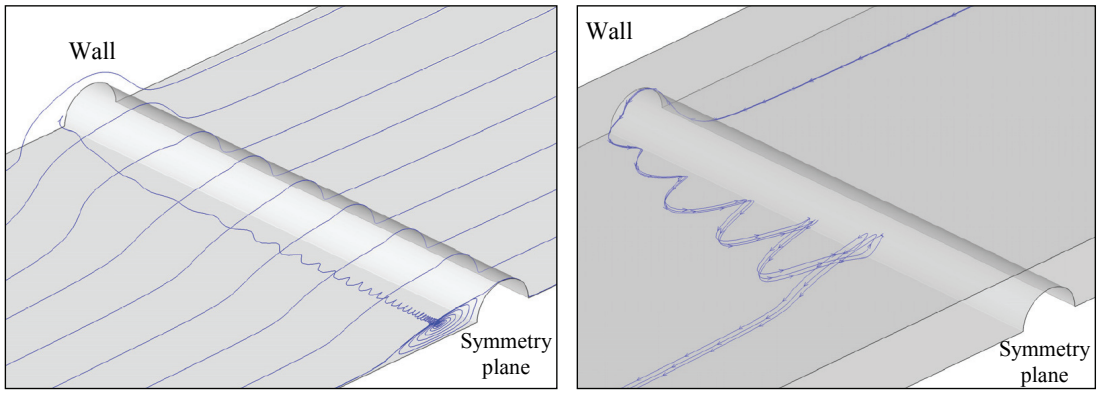

(a) (b)

Figure 9 - Streamtraces of particles near the cylinder for $AR = 8$ and $Re = 40$.

A final observation needs to be explained, the increase in L_v at the side wall. The boundary layer arguments invoked above that a low velocity fluid is able to negotiate better the cylinder and recover pressure more efficiently are valid when the fluid particles are not too close to the side wall. The side wall drains a significant amount of kinetic energy from the fluid particles, so even though

the local Reynolds number is lower the local energy dissipation hinders the capability of fluid particles to negotiate the cylinder and the outcome is a very sharp increase in L_v near the wall.

4. Conclusions

A combined experimental and numerical investigation was carried out on the laminar steady flow around a cylinder confined in a rectangular duct to assess the effects of finite aspect ratio. The blockage ratio was constant at 50%, the aspect ratio of the duct varied between 1 and 16 and the Reynolds number was varied between 0 and 40. The experiments relied on flow visualizations and detailed velocity measurements by PIV, whereas the numerical predictions were carried out with a finite volume numerical method. The numerical predictions compared very well with the experiments and consequently they were used to investigate in detail flow conditions that were not measured and to help interpret the results.

Velocity peaks near the side walls were found to occur at all Reynolds numbers and for large aspect ratios. At low Reynolds numbers these velocity peaks are due to the excessive braking role of the side wall, which forces a local fluid acceleration for mass conservation which the very small diffusive spanwise-streamwise momentum flux (τ_{xz}) is unable to smooth out. This peak disappears when the aspect ratio is reduced and by implication the τ_{xz} stress increases strongly. Inertia counteracts the role of this diffusive momentum flux so much that at $AR = 1$ and $Re = 40$ there are still velocity peaks. When inertia is strong there is flow separation in the wake of the cylinder, but this separated flow region is open. The fluid particles near the side wall, but not too near, are better able to sustain the adverse streamwise pressure gradient and better recover the pressure as they flow across the cylinder. Consequently, the separated flow region is shorter and the pressure is higher leading to a secondary spiraling spanwise flow from the side wall to the centre plane. The fluid exits this region at the centre plane and enter it at the velocity peak region which is being fed by fluid coming from the neighbor region located to the inner side of the duct. This has a positive feedback, enhancing the velocity peaks while simultaneously depleting the neighbor region of fluid creating a small region with a velocity deficit and less ability to sustain the adverse pressure gradient (slight longer recirculation next to the region of minimum L_v). On the other side of the velocity peak region, at the wall itself, friction extracts so much energy from the fluid particles that these are significantly less able to sustain the adverse streamwise pressure gradient and the separated flow length increases dramatically.

Acknowledgements

The authors acknowledge the financial support from FEDER and Fundação para a Ciência e a Tecnologia (FCT) through projects POCI/EQU/59256/2004 and POCI/EQU/56342/2004. P.C. Sousa also acknowledges the financial support from FCT through scholarship SFRH/BD/28846/ 2006. P.M. Coelho acknowledges the Department of Mechanical Engineering for the sabbatical leave.

References

Alves M.A., Oliveira P.J. and Pinho F.T. (2003) A convergent and universally bounded interpolation scheme for the treatment of advection. Int. J. Numer. Meth. Fluids 41: 47-75.

Alves M.A., Pinho F.T. and Oliveira P.J. (2001) The flow of viscoelastic fluids past a cylinder:

finite-volume high-resolution methods. J. Non-Newt. Fluid Mech. 97: 207-232.

Anagnostopoulos P., Iliadis G. and Richardson S. (1996) Numerical study of the blockage effects on viscous flow past a circular cylinder. Int. J. Num. Meth. Fluids 22: 1061-1074.

Brown R.A. and McKinley G.H. (1994) Report on the VIIIth International Workshop on Numerical Methods in Viscoelastic Flows. J. Non-Newt. Fluid Mech. 52: 407-413.

Carey E.O.A. and Townsend P. (1991) Slow visco-elastic flow past a cylinder in a rectangular channel. Rheologica Acta 30: 58-64.

Ferreira H.E. (2006) Flow of Newtonian and viscoelastic fluids around cylinders: numerical investigation of three-dimensional effects". MSc thesis (in Portuguese), Faculdade de Engenharia da Universidade do Porto, Portugal.

Gerich D. and Eckelman H. (1982) Influence of end plates and free ends on the shedding frequency of circular cylinders. J. Fluid Mech. 122: 109- 121.

Issa R.I. and Oliveira P.J. (1994) Numerical predictions of phase separation in two-phase flow through T-junctions. Computers and Fluids 23: 347- 372.

Liu Y. (2008) Bifurcation phenomenon in the wake of a 3-D cylinder. Computers and Fluids 37: 724-732.

Norberg C. (1994) An experimental investigation of the flow around a circular cylinder. J. Fluid Mech. 258: 287-316.

Oliveira P.J., Pinho F.T. and Pinto G.A. (1998) Numerical simulation of non-linear elastic flows with a general collocated finite-volume method. J. Non-Newt. Fluid Mech. 79: 1-43.

Poole R.J., Escudier M.P., Afonso A. and Pinho F.T. (2007) Laminar flow of a viscoelastic shear-thinning liquid over a backward-facing step preceded by a gradual contraction. Phys. Fluids 19: 93101.

Verhelst J.M. and Niewstadt F.T.M. (2004) Visco-elastic flow past circular cylinders mounted in a channel: experimental measurements of velocity and drag. J. Non-Newt. Fluid Mech. 116: 301-328.

Williamson C.H.K. (1996) Vortex dynamics in the cylinder wake. Ann. Rev. Fluid Mech. 28: 477-539.